

# Outside the Wall: Hydrodynamics of Type I Supernovae Interacting with a Partially Swept-Up Circumstellar Medium

C. E. HARRIS<sup>1</sup> AND P. E. NUGENT<sup>2,3</sup>

<sup>1</sup>*Department of Physics and Astronomy, Michigan State University, East Lansing, MI 48824, USA*

<sup>2</sup>*Lawrence Berkeley National Laboratory, 1 Cyclotron Road, MS 50B-4206, Berkeley, CA 94720, USA*

<sup>3</sup>*Department of Astronomy, University of California, Berkeley, CA 94720-3411, USA*

## ABSTRACT

Explaining the observed diversity of supernovae (SNe) and the physics of explosion requires knowledge of their progenitor stars, which can be obtained by constraining the circumstellar medium (CSM). Models of the SN ejecta colliding with CSM are necessary to infer the structure of the CSM and tie it back to a progenitor model. Recent SNeI revealed CSM concentrated at a distance  $r \sim 10^{16}$  cm, for which models of SN interaction are extremely limited. In this paper, we assume the concentrated region is a “wall” representing swept-up material, and unswept material lies outside the wall. We simulate one-dimensional hydrodynamics of SNeIa & Ib impacting 300 unique CSM configurations using RT1D, which captures the Rayleigh-Taylor instability. We find that the density ratio between the wall and ejecta – denoted  $A_0$  or “wall height” – is key, and higher walls deviate more from self-similar evolution. Functional fits accounting for  $A_0$  are presented for the forward shock radius evolution. We show that higher walls have more degeneracy between CSM properties in the deceleration parameter, slower shocks, deeper-probing reverse shocks, slower shocked ejecta, less ejecta mass than CSM in the shock, and more mixing of ejecta into the CSM at early times. We analyze observations of SN 2014C (Type Ib) and suggest that it had a moderately high wall ( $10 \lesssim A_0 \lesssim 200$ ) and wind-like outer CSM. We also postulate an alternate interpretation for the radio data of SN 2014C, that the radio rise occurs in the wind rather than the wall. Finally, we find that hydrodynamic measurements at very late times cannot distinguish the presence of a wall, except perhaps as an anomalously wide shock region.

*Keywords:* Type Ia supernovae — Type Ib supernovae — stellar mass loss — circumstellar gas — shocks

## 1. INTRODUCTION

Supernovae (SNe) infuse their host galaxies with metals and energy (Tinsley 1980), accelerate particles (Blandford & Ostriker 1978), create compact objects (Staelin & Reifstein 1968; Cocke et al. 1969), and give us a way of measuring cosmic expansion (Wagoner 1977). Using them precisely and accurately for these purposes requires detailed knowledge of their stellar progenitors. In principle the progenitors can be directly identified from pre-explosion observations (Smartt 2009), however, most systems are too dim to do this (Bloom et al. 2012). Therefore, progenitors are typically constrained through circumstantial evidence that can be connected to theoretical models.

The circumstellar medium (CSM) fossilizes stellar evolution through the millennia before explosion, and is thus diagnostic of mass-loss and mass-transfer processes that are central to SN progenitor identification. The CSM is illuminated by the blast wave formed when the SN ejecta impact it. Using models of the shock propagation, this light can be translated into the structure of the CSM and ejecta.

Normal luminosity (i.e., not superluminous) Type I SNe are the focus of this work. SNeI lack hydrogen in their spectra because the progenitor lost its hydrogen envelope. The two groups of normal-luminosity SNeI are SNeIa (thermonuclear) and SNeIbc (core-collapse). SNeIa occur in binary star systems, and the primary mystery of their progenitors is the nature of the mass-donor companion star to the carbon-oxygen white dwarf that explodes (e.g., Maoz et al. 2014). The CSM of SNeIa gives us insight into the mass transfer process

and nature of the companion (e.g., Chomiuk et al. 2012). SNe Ibc may not occur in binary systems, although they likely do (e.g., Arcavi et al. 2010). The CSM of SNe Ibc tells us about the timescale and physical mechanism by which the outer envelope is lost (e.g., Weiler et al. 2002).

Discovered in increasing numbers and across all SN classes are SNe with dense CSM at  $\gtrsim 10^{16}$  cm, and an evacuated cavity within this distance. Unlike in the canonical interaction scenario that produces SNe IIn, the SN initially appears normal (non-interacting) while it traverses the evacuated cavity. Months after explosion, ejecta impact dense CSM and transform into an interacting SN. For this reason we refer to such scenarios as “delayed interaction.” We use the shorthand “SNe X;n” to refer to delayed-interaction events, where “X” gets replaced by the non-interacting/peak-light/original classification, “n” refers to narrow emission lines as for SNe IIn, and the semicolon represents the separation between non-interacting and interacting phases. The most famous supernova SN 1987A is an example of an SN II;n. SN 2014C is an SN Ib;n – albeit with some (perhaps  $\sim 0.03 M_{\odot}$ ) hydrogen left in its outer envelope (Milisavljevic et al. 2015) reminiscent of SNe IIb – whose interaction began around 100 days after explosion. SN 2014C has a remarkable dataset, with high-cadence radio observations throughout its evolution complemented by x-ray, optical, and infrared spectra. Examples of SNe Ia;n are SN 2002ic (Wood-Vasey et al. 2004), PTF 11kx (Dilday et al. 2012; Silverman et al. 2013; Graham et al. 2017), and SN 2015cp (Graham et al. 2019).

There are two enormous gifts in studying SNe I;n. First, that hydrogen lines in the spectra are clean tracers of the CSM. Second, that the non-interacting portion of the light-curve can be analyzed with existing light-curve analysis tools to derive the SN properties. This means the SN structure can be constrained in the shock modeling much better than is usually the case, breaking ejecta-CSM degeneracies.

Understanding the physical origin of CSM in SNe I;n whose dense ( $\sim 10^{-18}$  g cm $^{-3}$ ) CSM appears to lie at  $\sim 10^{16}$  cm is a challenge. Such an environment can be created by a sudden increase in the ram pressure of the mass being expelled by the star system. A nova eruption from the system is an example of such a process (Moore & Bildsten 2012; Dimitriadis et al. 2014). Another example is the switch from a slow wind to a fast one (e.g., Castor et al. 1975; Weaver et al. 1977; Ramirez-Ruiz et al. 2005). The eruptive models naturally build up mass at  $\sim 10^{16-17}$  cm, while models of “wind-blown bubbles” generally place the over-density at a larger distance ( $\sim 10^{18-19}$  cm). One challenge for both models is to explain the high mass ( $\sim 0.1 M_{\odot}$ )

of material that is observed to exist at these distances. Thus, while both eruption and wind avenues are broadly successful for creating detached CSM, they fail in detail. Common to both is a CSM structure shaped by the sweeping-up of an existing medium.

For SNe Ib, the wind-blown bubble scenario has been modeled throughout the decades (owing to their proposed relationship to Wolf-Rayet stars). Typically these models have applicability to SN remnants, since the walls are not impacted until decades or centuries post-explosion. Chevalier & Liang (1989) present analytic estimates for the evolution of the shock while it is in the wall. Dwarkadas (2005) explores one-dimensional numerical calculations of the formation of the wall and evolution of the SN through the cavity, wall, and outer medium. Although wind-blown bubbles are supposed to form at large radii, the basic CSM structure has been compacted down for bespoke models of specific SNe, e.g. for the SNe Ib;n 2001em and 1996cr (Chugai & Chevalier 2006; Dwarkadas et al. 2010). Even for this specific CSM formation scenario, a systematic numerical study resulting in quantitative relationships that can be applied to new SNe has not been carried out.

Here we study SNe Ia&Ib impacting CSM that has been partially swept into a “wall,” outside of which lies the original pre-swept medium, as in wind-blown bubbles or nova eruptions. Figure 1 illustrates this configuration. Our aim is to provide interpretation tools for future SNe or ensemble datasets. In this paper, we limit our scope to the hydrodynamic evolution of the shocks, leaving the radiation calculation to a sequel. Some observations directly probe the kinematic properties of the shock fronts, e.g., spectroscopic line profiles or very long baseline radio interferometry (VLBI). Most of these observations are interpreted in the self-similar/“mini-shell” framework of Chevalier (1982) (hereafter “C82”) which has been developed in many papers over the decades. Therefore we particularly compare the hydrodynamic evolution of our models to what one would derive from the mini-shell model given the SN and CSM properties. To summarize some of the important limitations of the mini-shell model: it is a solution only applicable while the reverse shock is in the outermost ejecta, assumes the ejecta and CSM are similar density, and does not apply to transient phases when the forward shock crosses into a new CSM profile (e.g., after crossing the wall).

Our models are the first to systematically explore with numerical simulations a many-pronged space of CSM properties through a suite of  $\sim 600$  unique simulations. This is also the first suite of one-dimensional interaction simulations to capture the Rayleigh-Taylor insta-

bility, using RT1D (Duffell 2016) – though, of course, only approximately. The Rayleigh-Taylor instability prevents artificial density discontinuities from occurring in nature; in numerical simulations, these discontinuities can complicate the analysis of simulations when working with a complex CSM structure (e.g., Chevalier & Liang 1989; Dwarkadas 2005). Throughout this paper, we highlight the SN Ib models because of the emphasis on wind-blown bubbles in the literature and the quality of the SN 2014C data.

The paper is organized as follows. In §2 we describe the free parameters of our model suite (see Figure 1) and the hydrodynamics code used to simulate the interaction. In §3 we present the properties of the shock fronts and shocked gas in our model suite, focusing on quantities frequently used in interpreting observations: shock radii, shock front speeds, ejecta deceleration, shocked mass, and amount of mixing between ejecta and CSM. We particularly focus on finding analytic relations to describe the evolution of these properties, comparing them to self-similar evolution, and looking for degeneracies between CSM parameters. In §4 we discuss the application of these results to observations in more detail, first considering SN 2014C VLBI observations to constrain the wall height and outer medium density profile, then reinterpreting SN 2014C radio observations that probe the wall extent, and concluding with comments on which hydrodynamic quantities are reliable records of the wall in VLBI observations. We leave a detailed comparison between this model suite and observations of delayed-interaction SNe I to the sequel paper on radiation signatures. In §5 we provide a summary.

## 2. SIMULATION DESCRIPTION

### 2.1. Initial Conditions

In this paper we investigate the interaction of freely expanding supernova ejecta with a circumstellar medium characterized by an innermost evacuated cavity terminating at a thin “wall” of material, outside of which is an extended, lower density medium that we call the “outer CSM.” Figure 1 illustrates the model parameters detailed in this section.

We ignore the evolution in the inner evacuated cavity, assuming that the low-density medium has a negligible effect on the wall and ejecta profiles.

For the ejecta, we assume free expansion  $v = r/t$  ( $v$  is velocity,  $r$  radius, and  $t$  time) and consider density profiles that approximate an SN Ia and an SN Ib with a broken power law. The broken power-law profile arises from the propagation of the explosion shock through the star, which itself has an approximately broken power-law structure, as derived in Chevalier & Soker (1989).

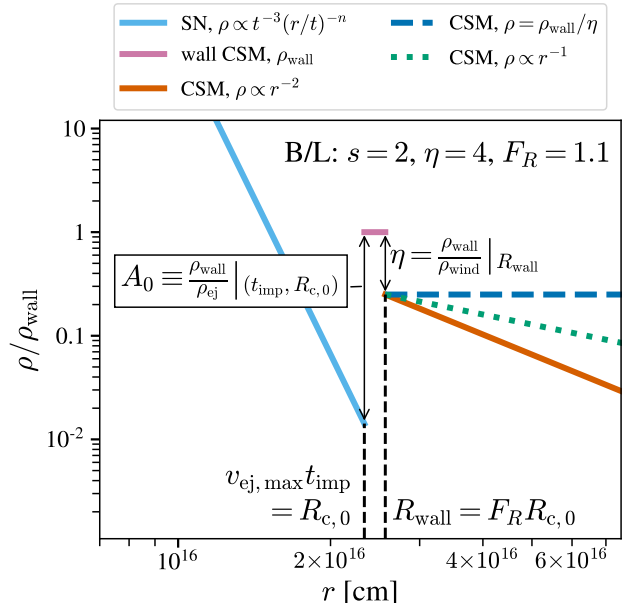


**Figure 1.** Definition of model variables and illustration of initial conditions. The baseline (B/L) CSM parameters are stated.

The outer regions have  $\rho_{ej} = g^n t^{n-3} r^{-n} \propto t^{-3} v^{-n}$ . The inner regions have a flatter density profile, which we model as  $\rho_{ej} \propto r^{-1}$ . The transition between inner and outer ejecta occurs at the transition velocity  $v_t$ . Density normalization factors and  $v_t$  are calculated using the expressions in Kasen (2010). For the SN Ia, we use  $n = 10$ , ejecta mass  $M_{Ia} = 1.38 M_\odot$ , and kinetic energy  $E_{ej} = 10^{51}$  erg (Harris et al. 2016). The SN Ib has  $n = 9$ ,  $M_{ej} = 1.7 M_\odot$ , and  $E_{ej} = 1.8 \times 10^{51}$  erg to be consistent with SN 2014C (Margutti et al. 2017). We truncate the ejecta at  $v_{ej,max} = 30,000$  km s $^{-1}$ , and simulations begin when the outermost ejecta reach the inner radius of the wall,  $R_{c,0}$ , at time  $t_{imp} = R_{c,0}/v_{ej,max}$ . We explore models with  $t_{imp} = \{30, 60, 90, 120\}$  days, which all have  $R_{c,0} \sim 10^{16}$  cm.

The wall has a constant density  $\rho_{wall} = \{10^{-18}, 3 \times 10^{-18}, 10^{-17}\}$  g cm $^{-3}$ , and the outer CSM has a density profile  $\rho_{csm} = qr^{-s}$  with  $s = \{0, 1, 2\}$ . The outer edge of the wall is located at  $R_{wall} \equiv F_R R_{c,0}$  with  $F_R = 1.01, 1.03, 1.1, 1.3$ . We take the density of the wall as proportional to the density of outer CSM at  $R_{wall}$ , as would be appropriate for a wall formed by a shock. The constant of proportionality is the compression ratio,  $\eta$ , and is given by the Rankine-Hugoniot strong shock jump conditions as

$$\eta \equiv \frac{\rho_{shocked}}{\rho_{unshocked}} \equiv \frac{\rho_{wall}}{\rho_{csm}(R_{wall})} = \frac{\gamma_{ad} + 1}{\gamma_{ad} - 1}, \quad (1)$$

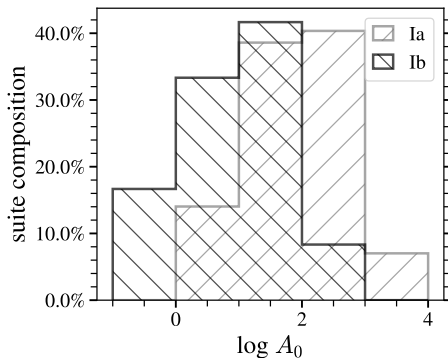


**Figure 2.** Representation of  $A_0$  values across all models, divided by SN type. Both types have the same CSM suite but the SN Ib ejecta are denser, shifting  $A_0$  to lower values.

where  $\gamma_{\text{ad}}$  is the adiabatic index. We explore compression ratios  $\eta = \{4, 7\}$ .

The ratio of the CSM density to the ejecta density at the point and time of impact is

$$A_0 \equiv \frac{\rho_{\text{wall}}}{\rho_{\text{ej}}(R_{c,0}, t_{\text{imp}})} \propto \rho_{\text{wall}} t_{\text{imp}}^3 \propto \frac{M_{\text{wall}} t_{\text{imp}}^3}{F_R^3 - 1}. \quad (2)$$

The  $A_0$  values covered by the suite are shown in Figure 2. This parameter is named for its analogy to the  $A$  parameter in C82, which is algebraically equivalent. The subscript zero is to indicate that it is at the initial time.

The variation in  $\rho_{\text{wall}}$ ,  $t_{\text{imp}}$ ,  $s$ ,  $\eta$ ,  $F_R$ , and SN class create a suite of 576 models. Since  $A_0$  depends only on  $\rho_{\text{wall}}$  and  $t_{\text{imp}}$ , each SN has 12 unique  $A_0$  values. When it is useful to narrow our focus in a demonstrative graph, we emphasize the SN Ib models. We also define the “baseline” (B/L) set of CSM parameters to be  $s = 2$ ,  $\eta = 4$ , and  $F_R = 1.1$ , to parallel the models posited for SN 1996cr and SN 2014C (Dwarkadas et al. 2010; Margutti et al. 2017).

## 2.2. Computational Method

We use the RT1D code (Duffell 2016) to model the hydrodynamics of the interaction. This is a moving-mesh Eulerian hydrodynamics code with a gamma-law equation of state (with  $\gamma_{\text{ad}} = 5/3$ ). We use the logarithmic spacing option to define the initial grid.

We ensured that the baseline set for both SN types was high enough resolution to obtain smooth curves in our analyses and sometimes call these “high-resolution” baseline models. By “high-resolution” we mean they were given 8000 zones instead of the 3000 zone limit applied to the rest of the suite. The spatial resolution  $\Delta x$  is not constant over the grid (logarithmic spacing) or in time (moving mesh). These models had significantly longer run times than a low-resolution counterpart, hence the restriction on non-baseline models,

which made the running of the entire suite feasible. Depending on the exact gridding, non-baseline models can still have comparable resolution to the baseline set.

The characterizing feature of RT1D is that it incorporates a one-dimensional prescription of the Raleigh-Taylor instability based on three-dimensional models. This instability is known to be common in SN interaction. Using this code, ejecta are able to mix with CSM, changing the composition of the shocked material, in contrast to the unmixed case. The fraction of CSM is tracked by the passive scalar  $X$ .

The gas pressures in our simulations imply very high gas temperatures, leading some to worry about the contribution from radiation pressure and accuracy of  $\gamma_{\text{ad}} = 5/3$ . However, this concern arises from intuition based on materials radiating as a blackbody, which our low-density gas does not (though the gas is mostly in a thermal velocity distribution). For blackbody radiation the radiation pressure ( $p_{\text{rad}}$ ) is proportional to the temperature ( $T$ ) as  $p_{\text{rad}} = aT^4/3$ , where  $a = 7.56 \times 10^{-15} \text{ erg cm}^{-3} \text{ K}^{-4}$  is the radiation density constant. Here instead we must return to the fundamental definition based on energy density,  $p_{\text{rad}} = u_{\text{rad}}/3$ , and calculate  $u_{\text{rad}}$  from the intensity ( $I_\nu$ ) which in the optically thin case is the integration of the emissivity ( $j_\nu$ ) along a path  $I_\nu = \int j_\nu ds$ . Performing the integrations over frequency and solid angle (assuming isotropic emission) yields  $p_{\text{rad}} = (1/3c) \int \varepsilon_{\text{ff}} ds \sim \varepsilon_{\text{ff}} \Delta R_{\text{shock}} / (3c)$ , in which  $c$  is the speed of light in vacuum,  $\Delta R_{\text{shock}}$  is the radial width of the shock, and  $\varepsilon_{\text{ff}}$  is the frequency-integrated power of free-free emission. For details of this calculation, we refer the reader to Rybicki & Lightman (1979). In all of these calculations the temperature is the electron temperature which may be lower than the gas (ion) temperature by a factor  $\lesssim 2000$  Ghavamian et al. (2007). For our estimate we will use the ion temperature and therefore overestimate the radiation pressure, since  $\varepsilon_{\text{ff}} \propto T^{1/2}$ . We find that for our models,  $p_{\text{rad}} \lesssim 10^{-4} p_{\text{gas}}$  therefore  $\gamma_{\text{ad}} = 5/3$  applies.

We investigated Bremsstrahlung cooling but found that the timescales are too long to be important, in line with Dwarkadas et al. (2010).

## 3. ANALYSIS

In this section we present our analysis of the shock hydrodynamics, focusing on quantities that have been used to interpret observations of interacting supernovae. Our methods for calculating these quantities are described in § 3.1.

We find that the evolution depends crucially on the parameter  $A_0$ , the initial density ratio between the CSM wall and the ejecta, as did Dwarkadas (2005). Keep in

mind that  $A_0$  is not strictly the density of the wall – the same density of CSM impacted at a later time will have a higher  $A_0$ .

Figure 3 shows a comparison of a low- $A_0$  (“low wall”) model to one with high- $A_0$  (“high wall”). Both models have baseline parameters  $s = 2$ ,  $\eta = 4$ , and  $F_R = 1.1$ . The x-axis is time normalized to  $t_{\text{imp}}$ , and the y-axis is radius normalized to initial contact radius. This figure demonstrates many of the themes explored in detail in our analysis.

The left panels show the time evolution of the pressure, from which the shock fronts are clearly distinguished. There is a steep gradient between shocked gas (bright/orange) and pre-shock gas (dark/purple) that is used to identify the shock fronts, which are shown as dashed lines in all panels. The forward shock front moves slower for higher walls – note that the y-axis range is smaller for the high-wall model. Crosses on the line of the forward shock front show the time at which the shock crosses the wall ( $t_{\text{xwall}}$ ), which occurs later for the higher wall. The trade-off is, that the reverse shock is much stronger for the higher walls – we see that there is actually a period of time when the reverse shock is moving inward radially in the higher wall model. In short, higher-wall models have a weaker/slower forward shock and stronger reverse shock than lower-wall models. Analysis of the shock front radii and speeds is presented in § 3.2-3.4.

The central panels show the gas velocities. Initially, all CSM moves at  $100 \text{ km s}^{-1}$  while ejecta are in free expansion and have a maximum velocity of  $30,000 \text{ km s}^{-1}$ . The shocked gas in the higher-wall model is much slower than in the lower-wall model. High walls have more stopping power than low walls, and we see that the reverse shock is reaching farther into the ejecta and probing lower velocities. This means the reverse shock of higher-wall models will cross into the dense inner ejecta faster than lower-wall models. Analysis of ejecta deceleration can be found in § 3.5.

The right panel shows the fraction of gas that is CSM material. Because our study uses RT1D, the ejecta and CSM mix due to the Rayleigh-Taylor instability. Dotted lines show where the composition is 5% and 95% CSM to give a sense of the boundary between mixed and unmixed material. (In our later analysis of mixing, we use a boundary of 1% to define mixed material.) The amount of mixing depends on the height of the wall and time of the simulation. Analyses of the amount of mass shocked and amount of mixing can be found in § 3.6 & 3.7.

### 3.1. Methods

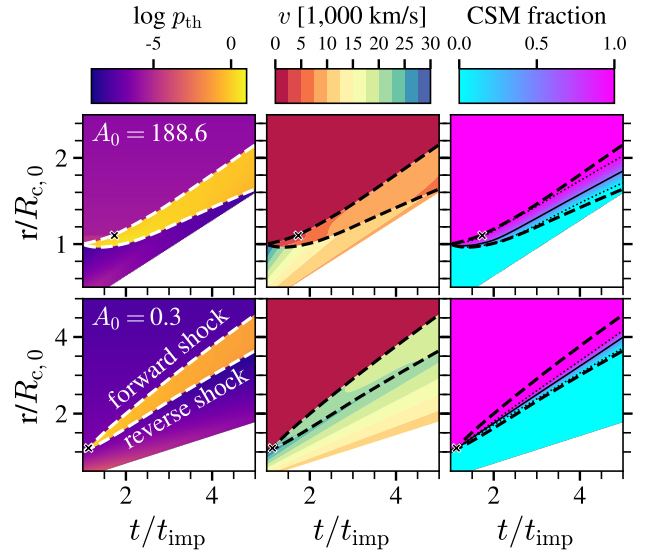


**Figure 3.** The evolution of a low- $A_0$  model (bottom) and high- $A_0$  model (top) from the baseline set, in radial coordinates. Note the smaller y-axis range in top panels. Dashed lines show shock fronts, and “x” marks  $t_{\text{xwall}}$ . *Left.* The common logarithm of pressure (units  $\text{erg cm}^{-3}$ ), used to find shock fronts. Notice that the higher wall produces a stronger reverse shock that initially moves inward. *Middle.* Gas speed. Notice the lower shocked gas speeds in the higher wall model and that the shock travels deeper into the ejecta, both effects of the wall’s increased stopping power. *Right.* Fraction of gas that is CSM, with  $X = 0.5$  (solid) and  $X = 0.05, 0.95$  (dotted) delineated.

*Identifying Shock Fronts*—We denote the forward and reverse shock radii as  $R_{\text{fwd}}$  (or  $R_f$ ) and  $R_{\text{rev}}$  (or  $R_r$ ), respectively. We identify the forward and reverse shock fronts as the locations of maximum magnitude in the radial gradient of the common logarithm of the thermal pressure, on either side of the ejecta/CSM interface. In one-dimensional models without mixing, the ejecta/CSM interface is defined by a contact discontinuity in the mass density. We do not have this discontinuity, and define the interface as the location where the CSM fraction is half.

RT1D is particularly suited to capturing shock fronts, and we found  $< 1\%$  difference in the determination of the forward and reverse shock radii with low resolution compared to high resolution. For the baseline CSM parameters, we only present high-resolution results.

In some models with low  $A_0$  we have observed that the rarefaction wave that propagates into the shocked ejecta (after the forward shock crosses from the wall into the lower-density outer CSM) steepens into a shock and does not overtake the original reverse shock front, creating a double-shock structure at late times. Once the rarefaction shock is as steep as the reverse shock,

our shock finding algorithm identifies this front since it is nearer to the interface.

*Calculating Shock Speeds*—The “lab-frame” shock front speeds are measured directly from computed radii using a second-order-accurate finite-difference solution for the first derivative accessed through the `numpy.gradient()` function. We refer to the lab-frame shock speeds as  $\dot{R}_{\text{fwd/rev}}$  (forward/reverse shock). The calculated velocities “jitter” due to the discretization of the temporal and spatial domains.

*Calculating Ejecta and CSM Masses*—The density is assumed constant in each cell, and is multiplied by the volume of the cell to get the mass of each cell in the domain. RT1D gives the cell extent as an output and the cell volume is calculated as  $V_i = 4\pi/3(r_i^3 - (r_i - \Delta r_i)^3)$ . To separate the mass into “CSM” and “ejecta”, the cell masses are multiplied by the CSM fraction in the cell (ejecta mass calculated by subtracting CSM mass from total). The cell masses can then be summed, e.g., only over the cells of shocked gas to get the total mass of shocked material.

*Fitting to Simulation Data*—Fits to simulation data described in the analysis were carried out with the `scipy.optimize.curve_fit()` routine.

### 3.2. Evolution of forward shock radius

Figure 4 shows the evolution of forward shock radius while it is inside the wall for baseline SN Ib models. Models of different  $\eta$  and  $s$  are not shown, as the curves would be the same. Color corresponds to the  $A_0$  parameter. Markers show the time of snapshots and their shape denotes the density of the wall. The black dashed line shows the self-similar solution, which the lowest- $A_0$  models are approaching. The remaining dashed lines show a fit to these data, described below.

The governing parameter for the evolution of shock radius is  $A_0$ . It is intuitive that a higher-density wall would lead to a slower shock. But one must be careful, what matters is not the absolute density of the wall but rather its density *compared to* the ejecta density — note from the marker shapes that walls of different absolute densities can have the exact same  $R_{\text{fwd}}(t)/R_{\text{c},0}$  if they have the same  $A_0$ .

These curves can be described by an integrated power-law whose parameters depend on  $A_0$ . In § 3.4 we demonstrate that the evolution of forward shock velocity while in the wall is nearly a power-law  $v_{\text{fwd}} = v_{\text{fwd},0}(t/t_{\text{imp}})^{m-1}$ , with  $m$  depending on  $A_0$ . Then  $R_{\text{fwd}}(t)$  should be described by its integral,

$$\frac{R_{\text{fwd}}}{R_{\text{c},0}} = \frac{v_{\text{fwd},0}}{v_{\text{ej,max}}} \left( \frac{t}{t_{\text{imp}}} \right)^m + \left( 1 - \frac{v_{\text{fwd},0}}{v_{\text{ej,max}}} \right), \quad (3)$$

where we have used the boundary condition  $R_{\text{fwd}}(t = t_{\text{imp}}) = R_{\text{c},0} = v_{\text{ej,max}}t_{\text{imp}}$ . Fitting this function to the data we can extract the best-fit values of  $v_{\text{fwd},0}/v_{\text{ej,max}}$  and  $m$  (terms are collected in the fitting equation). The best-fit values for each simulation in the suite are shown in Figure 5 as a function of  $A_0$ , limited to fit results that gave a maximum deviation between the data and fit of  $< 0.1\%$ , which we found is effectively a cut on spatial resolution. The left panel shows the power-law slope  $m$  and the right panel shows the initial shock speed — recall that  $v_{\text{ej,max}}$  is fixed to  $30,000 \text{ km s}^{-1}$  for our simulations (§ 2). In these panels, diamonds and stars denote SN Ib and SN Ia models, respectively. The large, filled markers are from the high-resolution baseline set, with fill color corresponding to  $A_0$  simply to further highlight them in the figure. For these points we show the fit errors, the square root of the covariance matrix diagonal elements, though they are typically smaller than the marker size. Unfilled, smaller markers represent models outside the baseline set. We include them to investigate the scatter caused by spatial resolution — since this fit is only to the in-wall portion of the shock evolution, the variation in  $s$ ,  $\eta$ , and  $F_R$  should not affect the fit results. As  $A_0$  decreases,  $v_{\text{fwd},0}$  increases, and is higher than  $v_{\text{ej,max}}$  for  $A_0 < 1$  (ejecta higher density than wall). As can be seen from the way we expressed the  $R_{\text{fwd}}/R_{\text{c},0}$  function, the result of higher  $v_{\text{fwd},0}$  is that the second term disappears and the shock radius evolves as purely a power-law in time, just like in the self-similar case. In fact, it is for this reason that we have chosen the variable  $m$ , since it is common in self-similar evolution applications to write  $R \propto t^m$ , and refer to  $m$  as the “deceleration parameter.”

In future, one may wish to use the  $m$  and  $v_{\text{fwd},0}$  values shown in Figure 5 and Equation 3 — or its derivative — when interpreting observations (example in § 4.2). As a convenient alternative to reading  $m$  and  $v_{\text{fwd},0}$  values off these plots, we offer the approximations  $m = 0.86A_0^{0.177}$  and  $v_{\text{fwd},0} = (25,600 \text{ km s}^{-1}) A_0^{-0.56}$ , which we found by fitting first-order polynomials to the base-10 logarithm of the quantities, fitting both SN types together since there is not more scatter between types than within a given type.

Figure 6 shows the evolution of the forward shock radius while the shock is in the outer CSM, varying the outer CSM properties  $s$ ,  $\eta$ , and  $F_R$  in turn about baseline values  $s = 2$ ,  $\eta = 4$ , and  $F_R = 1.1$ . For clarity, only the maximum, minimum, and median values of  $A_0$  are shown in this plot with values annotated in the left panel.

By  $t/t_{\text{imp}} = 3$ , models can be fit by  $R_{\text{fwd}} \propto t^m$ , but  $m$  depends on the CSM parameters. To investigate this systematically and determine which parameters have the

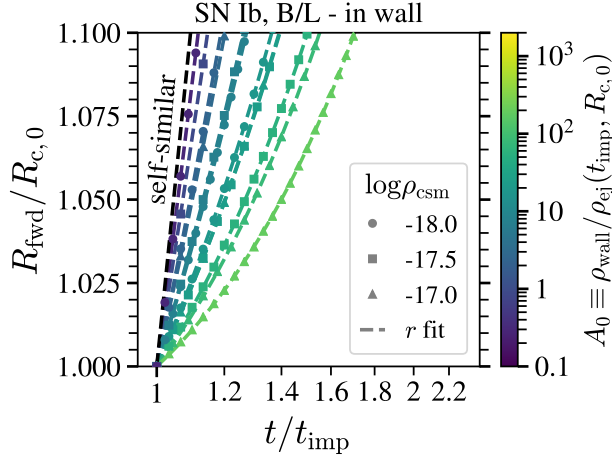


**Figure 4.** Evolution of forward shock radius while within the wall for SN Ib models ( $A_0 = 0.3 - 188.6$ ). Marker shapes denote wall density, in units of  $\text{g cm}^{-3}$  (value in legend), to show that  $A_0$  is the governing parameter of the curve shape. Dashed lines in the  $A_0$  color show the fit discussed in the text. The dashed black line shows self-similar evolution for reference.

maximum effect, we fit all models in the suite at times  $t/t_{\text{imp}} \geq 3$ . The median difference between the power-law fit and the actual data is  $< 1\%$  for all models. The result is shown in Figure 7. In this figure, color family shows  $s$  (red is  $s = 2$ ; green,  $s = 1$ ; blue,  $s = 0$ ), saturation shows  $\eta$  (light is  $\eta = 7$ , dark is  $\eta = 4$ ), and line style shows  $F_R$  (see legend). The span of the plots is the same to allow for comparison between the SN types. The C82 values for the power-law slope are shown for  $s = 0, 2$  as right arrows for reference. For  $s = 0$  the arrows can be plotted at  $A_0 = A$ , but for  $s = 2$ ,  $A = 0.096, 0.067$  (for SN Ib, Ia) are outside the span of the plot and are plotted at the left edge.

As  $A_0$  increases, the parameters become degenerate. Yet the deceleration parameter is a useful probe of the CSM (or ejecta) density profile when  $A_0$  is low – in that case, different values of  $\eta$  and  $F_R$  converge and  $m$  values are separated by  $s$ . However, by  $A_0 \sim 10$  the separation is lost, and a single value of  $m$  can be traced to a variety of CSM parameters, thus negating the interpretive importance of  $m$  alone.

### 3.3. Width of the Shock Region

One key feature of self-similar evolution is that the shock front locations are a constant multiple of the contact discontinuity radius and therefore the fractional width of the shock

$$\frac{\Delta R}{R_{\text{fwd}}} = 1 - \frac{R_{\text{rev}}}{R_{\text{fwd}}} \quad (4)$$

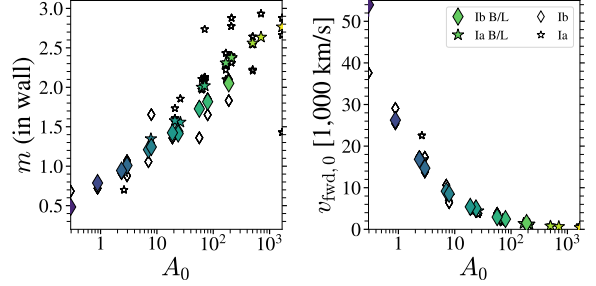


**Figure 5.** Fit parameters for  $R_{\text{fwd}}(t)$  as a function of  $A_0$  for the full model suite. Outer CSM parameters are irrelevant for this phase of the evolution, so scatter reflects temporal and spatial resolution.

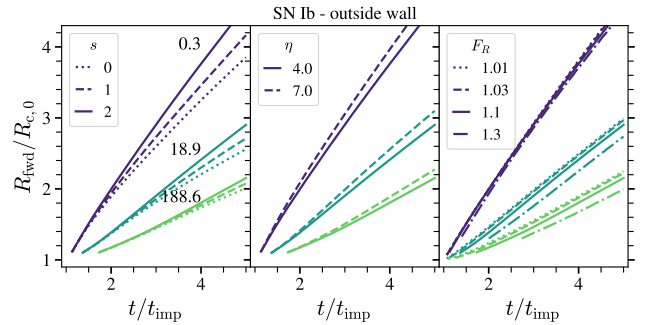


**Figure 6.** Evolution of forward shock radius while in the after  $t_{\text{xwall}}$ , changing the three outer CSM parameters in turn. Solid lines are baseline values.

is also a constant. Figure 8 shows that in our models, however, this is not the case. This figure is structured the same way as Figure 6, with color showing  $A_0$ , line style indicating different values of a CSM parameter, and different CSM parameters are changed in each panel. The full time span ( $1 \leq t/t_{\text{imp}} \leq 5$ ) is shown, and crosses show  $t_{\text{xwall}}$ . Black dashed lines show the self-similar values.

We find that the shock width generally grows quickly at first, but settles to  $\sim 20\%$  by  $t/t_{\text{imp}} \sim 2$ . There is no obvious dependence of the shock width on  $A_0$ ,  $s$ ,  $\eta$ , or  $F_R$ . Interpretation of observations prior to the asymptotic phase should account for the fact that the shock region is likely much thinner even than the mini-shell may predict, but at later times the typical assumption of  $\sim 10\%$  is a decent approximation.

For some low- $A_0$  models, the thickness seems to drop suddenly at  $t/t_{\text{imp}} \sim 3$ . This is because of the shock front finder identifying the rarefaction shock front instead of the reverse shock front, as described in § 3.1.

### 3.4. Shock Speeds

Figure 9 shows the evolution of the forward (top) and reverse (bottom) shock speeds throughout the duration of the simulation for baseline SN Ia & Ib models (thin

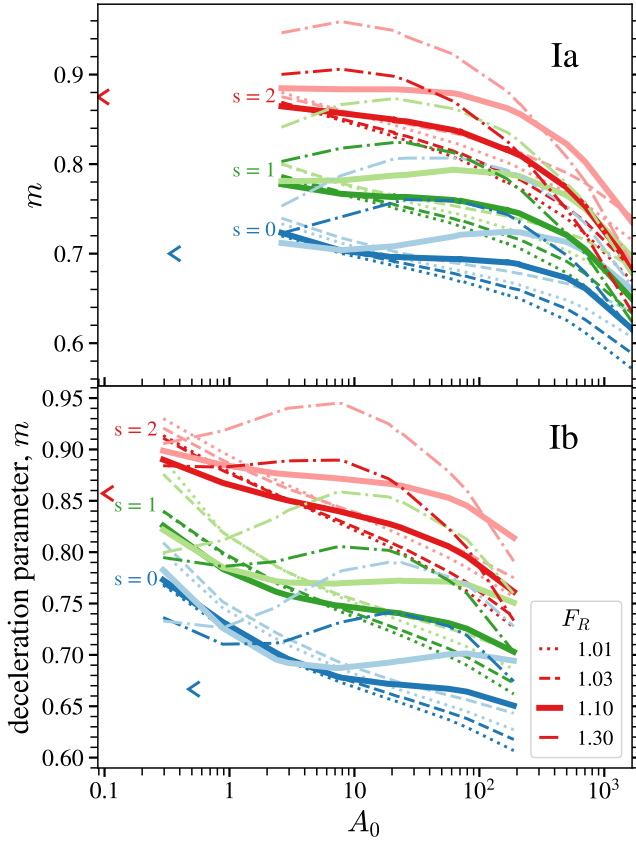


**Figure 7.** Power-law index  $m$  of  $R_{\text{fwd}} \propto t^m$  found by fitting the  $3 \leq t/t_{\text{imp}} \leq 5$  phase of the radius evolution, as a function of  $A_0$ , for the entire suite of SN Ib (bottom) and SN Ia (top) models. Line style shows  $F_R$  (see legend), color family indicates  $s$  (see annotations), and saturation denotes  $\eta$  (higher shades are  $\eta = 7$ ). Arrows indicate the mini-shell value.

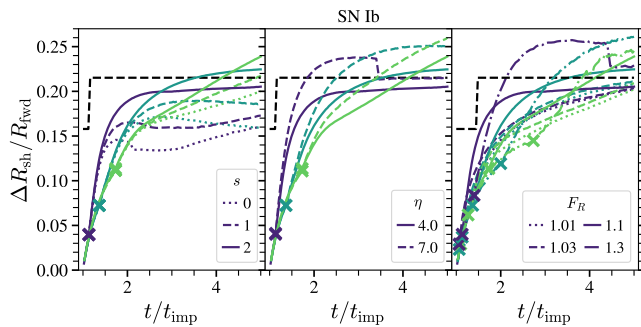


**Figure 8.** Fractional width of the shock region. Cross markers indicate  $t_{\text{xwall}}$ . Panels and colors are as in Figure 6. There are no clear trends with variations in CSM configuration, the shock width quickly grows to  $\sim 0.2R_{\text{fwd}}$  for all models. Self-similar value shown as black dashed line.

and thick lines, respectively). The time that the shock crosses into the outer CSM,  $t_{\text{xwall}}$ , is marked by an “x”. Curves are color-coded by  $A_0$ , with highest  $A_0$  having the lowest shock speeds. The black dashed line shows the self-similar solution for the CSM of the lowest- $A_0$  model.

In contrast to self-similar evolution, most models actually have an accelerating forward shock in the wall. In the self-similar regime, shocks do not accelerate unless  $s > 3$ . The forward shock speed while the shock is in the wall is fit very well by a power law

$$v_{\text{fwd}} = v_{\text{fwd},0} \left( \frac{t}{t_{\text{imp}}} \right)^{m-1}. \quad (5)$$

The  $m$  derived from fitting this function to the in-wall portion of  $v_{\text{fwd}}$  yields the same results as presented in Figure 7 from fitting its integral to the radius evolution – in § 3.2 we offer power-law fits for  $m(A_0)$  and  $v_{\text{fwd},0}(A_0)$ , for convenience. The shock is accelerating ( $m > 1$ ) for  $A_0 \gtrsim 10$ .

After  $t_{\text{xwall}}$ , the forward shock is in the outer CSM, which for the baseline set has a wind-like density profile. The self-similar line describes the velocity evolution in the outer CSM very well for low walls (low  $A_0$ ) but does not suit well for high walls until later times. As a rule of thumb, we find that self-similar evolution may be used at times later than the time at which  $\rho_{\text{ej}}(R_{\text{c},0}) = \rho_{\text{wall}}$ .

### 3.5. Deceleration of Ejecta

Figure 10 shows the evolution of shocked ejecta speed ( $u_{\text{ej}}$ ) over time for three baseline models representing the span of  $A_0$  – minimum, median, and maximum values. In case the colors denoting  $A_0$  are not distinct to the reader, we note the lowest  $A_0$  value is always the highest-speed curve (for any line style). The shaded band shows the minimum and maximum values of  $u_{\text{ej}}$  across cells of shocked ejecta. Noise in these curves is an effect of the steep velocity gradient near the reverse shock front and the resolution of the simulations. To minimize numerical noise we focus on the volume-average shocked ejecta speed,  $\langle u_{\text{ej}} \rangle_V$ , shown as a solid curve.

The stopping power of the wall can be illustrated by a comparison of the shocked ejecta speed to the speed of the ejecta crossing into the shock region ( $R_r/t$ , dashed lines). It is obvious that a higher wall (higher- $A_0$  model) is able to slow the ejecta much more than a lower wall. Given that the CSM speed is  $100 \text{ km s}^{-1}$ , the highest wall has effectively stopped the ejecta. After the forward shock has traversed the wall, however, the wall rarefies and moves outward and so the ejecta are able to be accelerated by the fast material still pushing from behind. The shocked ejecta reach some maximum speed  $u_{\text{ej,max}}$  and then begin to decelerate.

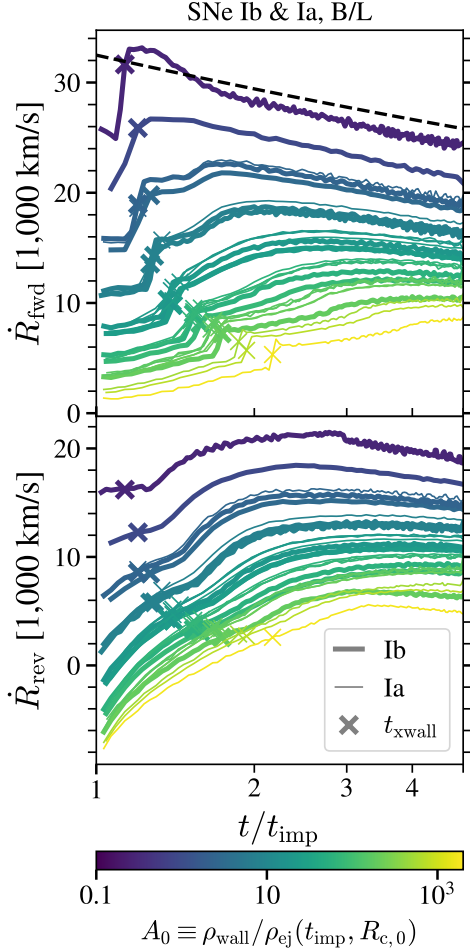


**Figure 9.** Forward (top) and reverse (bottom) shock speeds for baseline CSM models. Wall crossing time is indicated by an “x.” The black dashed line in the top panel shows the self-similar value for the lowest- $A_0$  simulation.

In fact, once in the decelerating regime the shocked ejecta speed is similar to the mini-shell prediction for evolution in the outer CSM density profile (dash-dotted lines), which can be calculated from Equation 21 of C82. Here, we will deviate from the original notation by using subscripts “f” in place of “1” (forward shock) and “r” in place of “2” (reverse shock). We assume  $R_r/t$  for the pre-shock velocity of the ejecta. The variable  $u_r/f$  will be used to refer to post-shock gas speed at the reverse/forward shock front. Using the constancy of  $u_r/u_f$ ,  $R_c$  given by Equation 3 of C82, and  $R_r/t = (R_r/R_c)(R_c/t)$ ,  $u_r$  is found to be:

$$u_r = \frac{3}{4} \left( \frac{n-3}{n-s} \right) \left( \frac{u_r}{u_f} \right) \left( \frac{R_f}{R_c} \right) \left( \frac{Ag^n}{q} \right)^{\frac{1}{n-s}} t^{(s-3)/(n-s)} \quad (6)$$

The parameter  $A$  is fixed for given  $n$  and  $s$ . The variables  $g^n$  and  $q$  are the normalizations of the density profiles, as in § 2. The cautious reader may note from C82

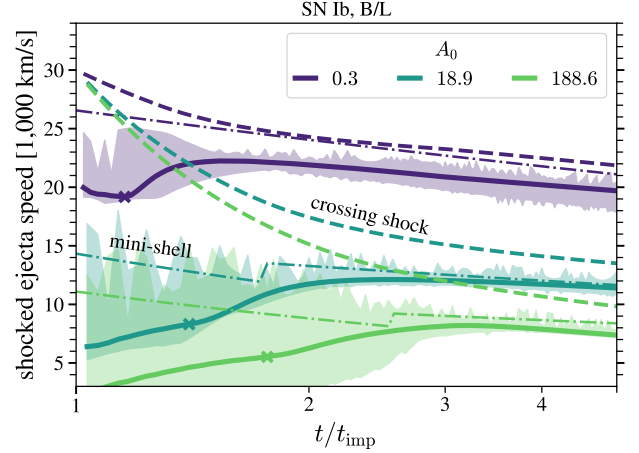


**Figure 10.** Shocked ejecta speed over time for three  $A_0$  values – baseline SN Ib. Solid lines are volume-average and envelopes show min./max. Dashed curves show the speed of the ejecta crossing the shock front. Dash-dotted curves show the mini-shell value. Time  $t_{\text{xwall}}$  is marked by “x.” Higher- $A_0$  walls decelerate the ejecta significantly more than low- $A_0$  walls and more than self-similar.

that gas velocity decreases between the reverse and forward shocks, so  $\langle u_{\text{ej}} \rangle_V < u_r$ . However, due to the thinness of the reverse shock region ( $(R_c - R_r)/(R_f - R_r) = 0.063$ ),  $u_{\text{ej}}$  is effectively constant in the mini-shell model. For  $s < 3$  the ejecta will be constantly decelerated by the CSM and therefore the maximum speed is achieved at  $t/t_{\text{imp}} = 1$ , unlike in our models whose maximum speed is later even than  $t_{\text{xwall}}$ . As in § 3.4, peak speed occurs when the reverse shock reaches ejecta of approximately the wall density.

Emission line widths for interacting SNe are often used as a proxy for the bulk velocity of shocked gas (e.g., for delayed interaction, Dilday et al. 2012; Milisavljevic et al. 2015). Figure 10 shows that for delayed-interaction SNe, one may observe significant deceleration of ejecta by a modest mass of CSM that is nevertheless much more dense than the ejecta impacting it. This principle is independent of the exact CSM configuration we are presenting in this work: low line velocities do not necessarily indicate a CSM mass comparable to or exceeding the total ejecta mass, in delayed-interaction events. In the context of our model suite, the observed line widths of a few  $1,000 \text{ km s}^{-1}$  or lower would suggest that delayed-interaction SNe tend to occur with  $A_0 \gtrsim 100$ .

### 3.6. Mass of Shocked Material

Figure 11 shows how the masses of shocked ejecta (left) and CSM (middle) evolve with time, for baseline CSM models. Color indicates  $A_0$ , the initial density ratio between the CSM wall and the ejecta. Higher-mass

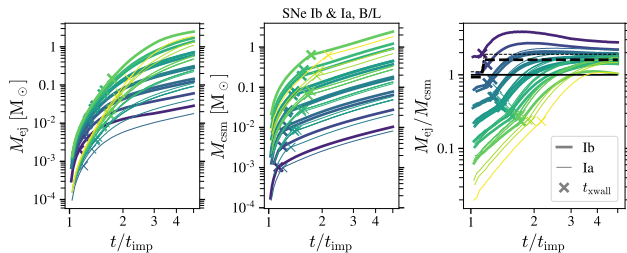


**Figure 11.** The masses of shocked ejecta (left) and CSM (center), and the ratio of shocked ejecta mass to shocked CSM mass (right). In the right panel, a solid black line shows unity and dashed black line shows the self-similar value. In all panels, “x” marks  $t_{\text{xwall}}$ .

curves have higher  $A_0$  values. Time is normalized to time of impact. The time the forward shock crosses the wall,  $t_{\text{xwall}}$ , is marked by an “x.” The right panel shows the ratio of shocked ejecta mass to shocked CSM mass (a proxy for the average composition of shocked material) with unity marked by a solid black line. The self-similar value is shown as a black dashed line.

The left and middle panels show that, for a given SN type, the mass swept up is the same for the same  $A_0$  values even though they represent different wall densities. This is because a lower-density wall farther away has a larger volume. Lower-wall models (lower  $A_0$ ) have lower shocked masses.

The mass of the wall is

$$M_{\text{wall}} = (2.1 \times 10^{-3} M_{\odot}) \rho_{\text{wall},-18} R_{c,0,16}^3 (F_R^3 - 1) \quad (7)$$

where  $\rho_{\text{wall},-18} = \rho_{\text{wall}} / (10^{-18} \text{ g cm}^{-3})$ ,  $R_{c,0,16} = R_{c,0} / (10^{16} \text{ cm})$ , and  $F_R$  can be either assumed or found by using  $t = t_{\text{xwall}}$  in Equation 3, recalling that  $m$  and  $v_{\text{fwd},0}$  depend on  $A_0$  (§ 3.2), which is set by  $\rho_{\text{wall}}$  and  $R_{c,0}$  (Equation 2).

Looking at how much of the shocked gas is ejecta (right panel), we see that the highest walls have the lowest ratio of ejecta to CSM mass. All models converge to an ejecta-to-CSM mass ratio of  $\sim$ few by late times. At early times, for high walls it is not a good assumption that approximately as much ejecta has been shocked as CSM – it can be up to  $t/t_{\text{imp}} = 3$  before that is the case.

### 3.7. Effect of Mixing

Unlike previous efforts to model interaction with CSM configurations similar to those we model, our simulations use a one-dimensional code that captures the mixing of ejecta and CSM in a way that approximates the behavior of three-dimensional shocks. The simulations are of course limited compared to nature in that they cannot reproduce the two-phase medium of hot and cold gas that the Rayleigh-Taylor instability is supposed to create and can impact observational signatures.

Interesting for observations is how polluted the CSM becomes from ejecta, which may have higher metallicity. For this analysis we consider “pure ejecta” to be gas with a CSM mass fraction  $X < 0.01$  and, likewise, “pure CSM” has  $X > 0.99$ . Thus, “polluted CSM” is gas with  $0.01 \leq X \leq 0.99$ . Figure 12 shows, for baseline CSM models, the percentage of shocked CSM mass that is polluted,  $100 \times M(0.01 \leq X \leq 0.99) / M(X \geq 0.01)$ . Thick lines show SN Ib models and thin lines show SN Ia models. Color is  $A_0$  and “x” shows the time the forward shock crosses the wall, as in other figures.

We find interesting diversity in the evolution of CSM pollution. Regardless of  $A_0$ , as the shock evolves in the outer CSM it will tend toward self-similar evolution with a healthy Rayleigh-Taylor instability and at least some mixing; but as with other hydrodynamical properties, the amount of time it takes for the self-similar solution to apply depends on  $A_0$ . For the highest walls, mixing increases while the shock is in the wall, even causing all of the wall mass to be polluted. Mixing stops when the shock crosses into the outer CSM, but the instability slowly gains strength again. For the lowest walls, mixing is unimportant in the wall phase but the instability grows as the shock traverses the outer medium. We see that  $\sim 60\%$  of shocked CSM is polluted material by the end of the simulation for the lowest wall, and that fraction is growing. In the range of intermediate wall heights, the behavior is somewhat complicated. Mixing seems to make a start when the shock initially crosses into the outer CSM, but is dampened, possibly by the rarefaction wave. The percent of polluted CSM grows faster in the outer CSM for lower walls. In summary, due to the different growth and damping timescales of mixing for different  $A_0$ , we find that high walls have mostly polluted CSM except at the earliest times, low walls have low CSM pollution until late times, and intermediate walls have moderate CSM pollution at all times.

The only general rule we offer is that at least 10% of shocked CSM seems to be polluted by ejecta material at the  $> 1\%$  level, across all  $A_0$  and  $t/t_{\text{imp}}$ . Thus when considering the composition of the shocked CSM for interpreting observations of interactions, one needs to account for  $A_0$  and the relative time of the observation, even for rough estimates. For any detailed analysis, of course, one would want to use the radial profile of the CSM fraction over time instead of the summary quantity we present here.

## 4. DISCUSSION

### 4.1. Application to Observations of SN 2014C

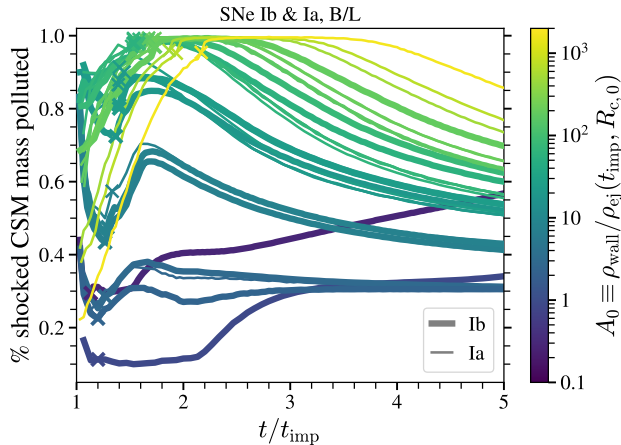


**Figure 12.** Fraction of shocked CSM mass that is a blend of ejecta and CSM. Crosses mark  $t_{xwall}$ .

Here we will apply our models to the observations of SN 2014C to demonstrate the application of our hydrodynamic results for determining CSM properties.

The properties of the SN ejecta are constrained from the early light curve in Margutti et al. (2017, hereafter, M17) and our SN Ib model is set up to be consistent with SN 2014C. The key observations are the impact time from radio and optical data, an estimate of the wall density from x-ray data, and measurements of the forward shock radius, deceleration parameter, and shock speed from very long baseline radio interferometry (VLBI). Putting these pieces together we constrain  $A_0$  and  $s$ .

The onset of interaction – i.e., initial impact with outermost ejecta – is not yet precisely constrained for SN 2014C. Interaction certainly began by 120 days post-explosion, based on the emergence of a  $\sim 1,000 \text{ km s}^{-1}$  H $\alpha$  emission line component in the optical spectra (Milisavljevic et al. 2015), and likely at about 100 days based on the flattening 15.7 GHz radio light curve (Anderson et al. 2017, hereafter, A17). For this discussion we also include  $t_{imp} = 190$  days (the assumption of both A17 and M17 based on the onset of radio rise), though it is unclear to us how to reconcile this  $t_{imp}$  with the strong H $\alpha$  emission already at 120 days. This brings the final list of possible impact times to  $t_{imp} = 100, 120, 190$  days. In our models  $R_{c,0} = (2.56 \times 10^{16} \text{ cm})t_{imp}/(100 \text{ days})$ , so for the three  $t_{imp}$  we are considering,  $R_{c,0} = (2.56, 3.07, 4.86) \times 10^{16} \text{ cm}$ , which are all consistent with the x-ray non-detection limit of M17.

We first attempt to estimate a range of reasonable  $A_0$  values for SN 2014C via  $\rho_{wall}$  and  $t_{imp}$  (Equation 2). Using the x-ray emission measure at 500 days to derive the number of emitting particles, and the volume of gas derived assuming self-similar evolution of the shock,

M17 derive  $\rho_{wall} \sim 10^{-17} \text{ g cm}^{-3}$ . We note this value depends on the assumed composition, and while M17 assumed solar abundances, our modeling shows a significant degree of pollution from the ejecta (Figure 12). A hypothesis we will explore in the sequel paper on radiation signatures is that the M17 density is over-estimated, and here we will consider  $\rho_{wall} = 10^{-18} \text{ g cm}^{-3}$  also possible. In our SN Ib suite, the model with  $\rho_{wall} = 10^{-17} \text{ g cm}^{-3}$  and  $t_{imp} = 120$  days is the highest- $A_0$  model with  $A_0 = 188.6$ . Scaling off of this using Equation 2, for  $\rho_{wall} = 10^{-17} \text{ g cm}^{-3}$  the impact times give values of  $A_0 = 110, 190, 750$  (rounding to the nearest ten). The  $\rho_{wall} = 10^{-18} \text{ g cm}^{-3}$  assumption has  $A_0$  a factor of ten lower than these values (11, 19, 75). Note that these values are all significantly above  $A_0 \sim 1$ , indicating the self-similar solution does not apply. One may notice that the inner radius assuming  $t_{imp} = 190$  days is nearer than derived in M17 ( $[4.9 \text{ vs. } 5.5] \times 10^{16} \text{ cm}$ ) because we define “beginning of interaction” differently – they assume the forward shock traversing the rarefied inner cavity can be transmitted through the wall, whereas we assume it is negligible and wait for the ejecta to reach the wall – and if we used their  $R_{c,0}$  rather than their  $t_{imp}$ , we would derive  $t_{imp} = 215$  days and  $A_0 = 1080$ .

For the nearest SNe, VLBI can be used to directly image the expanding shock fronts and measure hydrodynamical quantities like  $R_{fwd}$ ,  $\Delta R_{sh}$ , and  $v_{fwd}$ . Bietenholz et al. (2018, hereafter, B18) present interferometry of SN 2014C  $\sim 400 - 1000$  days after explosion. Given our range of  $t_{imp}$  values, the radio interferometry spans  $4 \leq t/t_{imp} \leq 10$  (minimum  $t_{imp}$ ) or  $2 \leq t/t_{imp} \leq 5$  (maximum  $t_{imp}$ ). At these phases of evolution, nearly all of our models have the forward shock already traversing the outer CSM, so the relevant figures for radial information are Figures 6 & 7. Measurements of  $v_{fwd}$  can be compared to the baseline model set with Figure 9.

The first quantity of interest from the VLBI measurement is the forward shock radius itself. B18 reports that at 384 days ( $3.32 \times 10^7 \text{ s}$ ),  $R_{fwd} = (6.4 \pm 0.3) \times 10^{16} \text{ cm}$ , corresponding to  $t_{VLBI}/t_{imp} = 3.84, 3.2, 2.02$  and  $R_{VLBI}/R_{c,0} = 2.5, 2.1, 1.3$ . Looking at Figure 6, these values all lie around the  $A_0 = 18.9$  model lines, independent of  $s$ ,  $\eta$ , or  $F_R$ .

Next, we look at the measurement of the deceleration parameter. In § 3.2 we mentioned that the deceleration parameter,  $m$ , is used to describe the radial evolution as  $R_{fwd} \propto t^m$  and showed that  $R_{fwd}(t/t_{imp} > 3)$  – when the shock is in the outer CSM – can be fit precisely with a power-law, but  $m$  depends on  $s$ ,  $\eta$ ,  $F_R$ , and  $A_0$  (Figure 7) and for even moderately high values of  $A_0$ , interpretation of  $m$  may be muddled. Fitting to the VLBI data, B18 find a best-fit  $m = 0.79 \pm 0.04$

for SN 2014C. Despite the confusion in the high- $A_0$  region of Figure 7,  $s = 0$  is disfavored – only  $F_R = 1.3$ ,  $\eta = 7$  models (with  $A_0 \lesssim 100$ ) have  $m > 0.75$ . Furthermore, assuming the sweeping up of the outer CSM occurred adiabatically and favoring  $\eta = 4$  models, then  $s = 0$  is ruled out, only the  $s = 1$ ,  $F_R = 1.3$  models with  $A_0 < 100$  are consistent with the data, but all  $F_R$  values are within the margin of error for  $s = 2$ . The wind-like outer medium favored by our model is in line with the analysis of Tinyanont et al. (2019), who found  $s = 2$  using the model of Moriya et al. (2013), which is self-similar but applies at these late times. Note that from the mini-shell solution  $m = (n - 3)/(n - s)$  with  $n = 9$  and  $m = 0.79$ , one would derive  $s = 1.4$ . Finally, for  $\eta = 4$ , the measured range of  $m$  suggests  $A_0 < 300$  independent of  $F_R$  and  $s$ , assuming the curves continue to decline.

Finally, we can compare our models to the shock velocity measured by B18. Our models only capture their first data point  $v_{\text{wd}} = 14,500 \pm 3,400 \text{ km s}^{-1}$  at  $t \sim 514$  days, which corresponds to  $t/t_{\text{imp}} \sim 5.1, 4.3, 2.7$ . In our baseline suite ( $s = 2$ ,  $\eta = 4$ ,  $F_R = 1.1$ , consistent with the constraints on SN 2014C from  $m$ ), models with  $A_0 \sim 3 - 200$  match the measured velocity given the measurement errors. The B18 measurements show a nearly constant velocity, which is most consistent with  $A_0 \gtrsim 20$  models (Figure 9).

In summary, the density ratio between the CSM and outermost ejecta for SN 2014C can be constrained by radio, optical, and x-ray data to be  $11 < A_0 < 750$  based only on the wall density (we discuss  $\rho_{\text{wall}} = 10^{-18}, 10^{-17} \text{ g cm}^{-3}$ ) and time of impact (we discuss  $t_{\text{imp}} = 100, 120, 190$  days). These values of  $A_0$  are all in the regime where self-similar solutions do not accurately approximate the hydrodynamics. Radio VLBI measurements have been reported for SN 2014C, though we can only use the earliest of the observations for direct model comparison. The measured radius at 384 days best matches models with  $A_0 \sim 20$  for the earlier  $t_{\text{imp}}$  and  $A_0 \sim 60$  for  $t_{\text{imp}} = 190$  days, independent of  $s$ ,  $\eta$ , or  $F_R$ . For any  $A_0 > 11$ , the measured deceleration parameter favors  $s = 2$  for the outer medium, and strongly disfavors  $s = 0$ , particularly if the wall was formed adiabatically such that  $\eta = 4$ . If both  $\eta = 4$  and  $s = 2$ , then for the baseline models ( $F_R = 1.1$ ), the measured shock velocity at 500 days is most consistent with models that have  $A_0 \sim 20$ , but  $3 \lesssim A_0 \lesssim 190$  are within the velocity and  $t_{\text{imp}}$  uncertainties. We conclude that, analyzing the SN 2014C VLBI observations within the context of our models and assuming  $\eta = 4$ , an  $s = 2$  outer medium is favored and models with  $\rho_{\text{wall}} \sim 10^{-18} \text{ g cm}^{-3}$  are consistent for the entire range of  $t_{\text{imp}}$ , but the  $\rho_{\text{wall}} \sim$

$10^{-17} \text{ g cm}^{-3}$  wall proposed by M17 is also within errors as long as  $t_{\text{imp}} \sim 100$  days rather than their assumed  $t_{\text{imp}} = 190$  days. Earlier impact times are also favored by the optical observations of interaction signatures by 120 days, and imply  $R_{\text{c},0} \sim 3 \times 10^{16} \text{ cm}$ , consistent with the x-ray non-detections of M17. The wind profile derived by Tinyanont et al. (2019) has a density  $1.15 \times 10^{-18} \text{ g cm}^{-3}$  at  $2.6 \times 10^{16} \text{ cm}$ , in line with our range of  $\eta$  and  $\rho_{\text{wall}}$ .

#### 4.2. A Reinterpretation of SN 2014C

Both the x-ray and radio emission of SN 2014C have maxima at  $t \sim 400 - 500$  days (A17, M17), and the x-ray emission measure indicates that the shocked CSM mass is  $1 - 1.5 M_{\odot}$  at this time; but what does this mean about the shock evolution?

M17 interpret the x-ray peak (they use  $t \sim 500$  days) to be the shock front passing over the CSM wall. Maintaining this assumption but using the earlier impact time of  $t_{\text{imp}} = 120$  days from optical observations, a model with  $A_0 = 50$  (in line with VLBI) has  $M_{\text{wall}} \approx 1.2 M_{\odot}$ , approximately the derived mass of shocked CSM from the x-rays. This wall would extend to  $R_{\text{wall}} \sim 6 \times 10^{16} \text{ cm}$  (similar to their derived  $R_{\text{wall}}$ ) but would have a lower density than they derived,  $\rho_{\text{wall}} \sim 2.7 \times 10^{-18} \text{ g cm}^{-3}$ . All wall models with  $M_{\text{wall}} = 1 - 1.5$  and the above interaction timings are similar – the allowed range is  $A_0 \sim 30 - 70$ , which sets  $F_R \sim 2 - 2.25$  and  $\rho_{\text{wall}} \sim (1 - 4) \times 10^{-18} \text{ g cm}^{-3}$ . Thus our models suggest a lower-density, thicker wall compared to M17, because the mass is maintained but the inner radius decreases.

Now we offer a more speculative extension of our hydrodynamic results that re-interprets the radio and x-ray peaks. Our re-interpretation stems from the fact that the shock speed determines the gas energy density and, for  $A_0 \gtrsim 10$  values, the shock speed peaks well after the shock has crossed the wall. We speculate that the radio rise may actually reflect the rapid rise of  $v_{\text{sh}}$  following the crossing of the wall, i.e.,  $t_{\text{xwall}} = 190$  days.

The optically thin radio luminosity depends strongly on shock speed. Using Equation 37 of Harris et al. (2016), the radio emissivity ( $j_{\nu}$ , units  $\text{erg s}^{-1} \text{ Hz}^{-1} \text{ cm}^{-3} \text{ sr}^{-1}$ ) is  $j_{\nu} \propto u_{\text{gas}}^3 \propto v_{\text{sh}}^6$ , assuming the gas energy density ( $u_{\text{gas}}$ ) is proportional to the square of the shock speed ( $v_{\text{sh}}$ ). The luminosity will depend on this factor, the volume of shocked gas, and the optical depth, which all depend on the shock speed for their time evolution, and should be dominated by changes in emissivity (optically thin regime) and optical depth (optically thick regime). Unpublished data indicate that the 15.7 GHz light-curve was optically thin at  $\sim 300$  days (A. Kamble,

priv. comm.), and, if the 15.7 GHz rise is optically thin, then it evolves like  $v_{\text{sh}}^6$ . The 15.7 GHz flux increased by a factor of  $\sim 6$  between 190 and 400 days (A17, Figure 1), requiring only a factor of  $\sim 1.35$  increase in  $v_{\text{sh}}$ .

The magnitude and timescale of increase in  $v_{\text{sh}}$  is matched by our models with a significantly lower wall mass than posited by M17. Allowing  $t_{\text{imp}} = 100, 120$  days,  $t_{\text{xwall}}/t_{\text{imp}} = 1.9, 1.6$  and  $t_{\text{peak}}/t_{\text{imp}} = 4, 3.3$ . From Figure 9 (models have  $F_R = 1.1, \eta = 4$ , and  $s = 2$ ) we see that the  $A_0 \sim 190$  model (highest  $A_0$  of the SN Ib set) has  $t_{\text{xwall}}/t_{\text{imp}} \sim 2$ , a peak speed at  $t/t_{\text{imp}} \sim 4$ , and an increase in shock speed of  $\sim 1.3$  between crossing and peak, which are all consistent with the 15.7 GHz light-curve under the optically thin assumption. The  $A_0 \sim 60$  models peak at  $t/t_{\text{imp}} \sim 3.25$  with a shock speed increase of  $\sim 1.4$ . This reinterpretation implies  $F_R = 1.25, 1.15$  and  $M_{\text{wall}} = 0.06, 0.04 M_{\odot}$  for  $A_0 = 20$  or  $F_R = 1.14, 1.08$  and  $M_{\text{wall}} = 0.31, 0.17 M_{\odot}$  for  $A_0 = 200$  (Equations 2, 3, & 7). At  $t \sim 500$  days the total mass of shocked CSM would be  $\sim 1 M_{\odot}$  (Figure 11,  $F_R = 1.1$  models), in agreement with the shocked CSM mass estimate of M17, but most of this mass is from the outer CSM, not the wall.

Thus we find that if we assume an impact time  $t_{\text{imp}} \sim 100$  days, we can re-interpret the M17 derivation of a shocked CSM mass  $1 - 1.5 M_{\odot}$  at 500 days in two ways. First, maintaining their assumption that  $t_{\text{xwall}} \sim 500$  days, we find the wall density must be  $\sim 2 - 10$  times lower than they report. However, we also posit  $t_{\text{xwall}} \sim 190$  days, and find this implies a wall  $\sim 5 - 40$  times less massive than they reported, and the mass at 500 days is primarily shocked wind material. In both cases, the range of values reflects uncertainty in  $A_0$  but implied  $A_0$  values are in line with the constraints from VLBI. Radiation transport calculations are required for calculations for detailed comparison to observations, including accurate interpretation of the radio rise and peak of SN 2014C, which we leave to our next publication on this model suite.

#### 4.3. Memory of the Wall

A wall of very limited extent may be crossed over by the forward shock very quickly, such that observations only probe the phase of evolution in the outer CSM or perhaps have a single epoch of observations in the wall phase. Or, for example, the hydrodynamics-probing observations of Bietenholz et al. (2018) could only be undertaken at late times because the method requires the shock to have a certain angular extent. Therefore, a crucial question is whether (and for how long) the exis-

tence of a wall can be inferred from observations after the wall-crossing time, i.e., how different is the evolution with a wall compared to with the outer CSM alone?

As an initial probe of this question, we removed the wall from the highest- and lowest- $A_0$  SN Ib simulations with  $s = 2$  and  $\eta = 4$  (baseline values), extended the outer CSM inward to maintain the impact time, and reran the simulation. Note that  $A_0$  is reduced by a factor of  $\eta$  in a wind-only model compared to the with-wall version, but we will refer to  $A_0$  values from the with-wall model. Because  $F_R$  affects the initial conditions of the shock front evolution in the outer CSM, we compare the wind-only simulation to with-wall simulations of all  $F_R$  values (1.01, 1.03, 1.1, and 1.3). We will be comparing the difference in hydrodynamic quantities between the no-wall models and their counterparts with a wall. We will compare the simulation differences to observational errors from VLBI of SN 1993J at late times Bartel et al. (2002) and SN 2014C that are likely at  $t/t_{\text{imp}} < 10$  according to our analysis (Bietenholz et al. 2018).

Figure 13 shows the comparison of no-wall models to models in the suite with the same outer CSM. Line style represents  $F_R$  as in Figure 7, color represents  $A_0$  as given in the legend and the same as in all other plots. The top panel shows the deviation in forward shock radius of the model without a wall from the model with a wall (black lines are 0% and 5%), and the bottom panel shows the same for the shock width (black line is 0%, grey band shows  $\pm 5\%$ ).

We find the percentage deviation between wall/no-wall models in forward shock radius (top panel) is small for most models. It is often comparable to observational error, which for SN 1993J was  $< 1\%$  and for SN 2014C  $3\% - 23\%$  (typically  $\sim 4\%$ ). We also looked at the deceleration parameter ( $m$ ) that would be measured in  $3 \leq t/t_{\text{imp}} \leq 5$ . We found that  $m$  fit to the model without a wall deviated from the wall model by  $(0.5 - 5)\%$ , depending on  $F_R$  and  $A_0$ . The errors on  $m$  reported for SN 1993J were  $(1 - 3)\%$  and for SN 2014C,  $\sim 5\%$ . Therefore it does not seem the measurements of  $m$  are precise enough to say whether a wall is present – and according to our analysis, interpretation of  $m$  is complicated anyway from other CSM parameters (§ 3.2, Figure 7).

The width of the shock region (bottom panel) does seem to be a potential probe of the presence of a wall. At most times, the shock region is thicker when a wall is present. This is in part because the forward shock radius, which we use to normalize the thicknesses, is higher in wind-only models. The other contribution is from the wall driving a stronger shock back into the ejecta, widening the shock region. The sudden change seen in the low- $A_0$   $F_R = 1.3$  model curve at  $t/t_{\text{imp}} \sim 4.5$

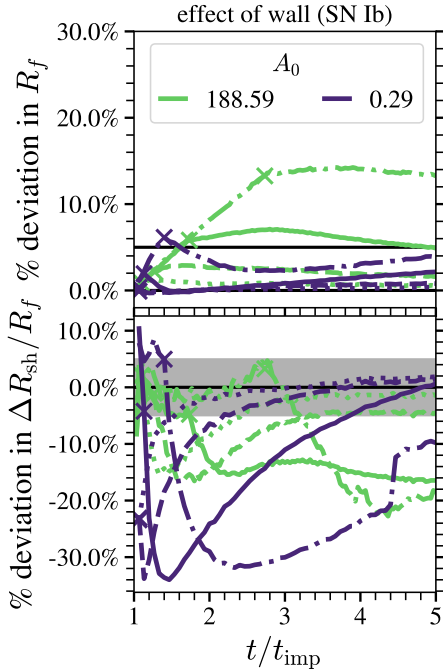


**Figure 13.** Comparison of model without the wall to the suite model with a wall for SN Ib. Line style shows  $F_R$  as in Figure 7. Color denotes  $A_0$  (see legend) and an “x” marker shows  $t_{xwall}$ . *Top.* Forward shock radius deviation,  $(R_{f,no-wall} - R_f)/R_f$ . *Bottom.* Shock thickness,  $(y_{no-wall} - y)/y$ , where  $y = \Delta R_{sh}/R_f$ .

is due to the shock front finder identifying a rarefaction wave, also seen in Figure 8, as described in § 3.1. Grey bands show 5% deviations, which is comparable to the precision of shock thickness measurements for SN 1993J, albeit at late times.

We conclude that for kinematic quantities about the shock, e.g., those probed by VLBI, observations would probably be equally well modeled by a cavity and wind as by a cavity, wall, and wind, with the wind having the same properties between both models. If the shock thickness can be measured, an anomalously thick shock region may indicate that the CSM had a wall.

However, other radiation signatures will likely be very different with or without a wall – Dwarkadas et al. (2010) noted that a wall was required to match the x-ray evolution of SN 1996cr, and in our own exploratory modeling of SN 2014C we found this to be the case as well.

## 5. SUMMARY

We explore the impact of a normal SN Ia or SN Ib with a circumstellar medium (CSM) that has been shaped by an eruption or change in wind properties – a smooth distribution of outlying mass is partially swept up into a “wall” of material at  $\sim 10^{16}$  cm. Our interest is con-

straining the CSM of canonical events like PTF 11kx or SN 2014C and providing a standard baseline for interpreting future events and observational ensembles. Through a suite of  $\sim 600$  one-dimensional models, we traverse a wider range of parameter space in CSM properties than any similar study yet undertaken. An overview of the parameters in this study is illustrated in Figure 1. Our baseline values are  $s = 2$  (outer medium is a wind),  $\eta = 4$  (the wall is formed by adiabatic compression of the wind in a strong shock), and  $F_R = 1.1$  (10% fractional extent of the wall). By running these simulations with RT1D we are able to study the effects of mixing due to the Rayleigh-Taylor instability at the interface of the shocked media, a well-known yet rarely captured effect in studies of supernova-CSM interaction. Since it is nevertheless a one-dimensional model, it does not capture the two-phase nature of the turbulent area, e.g., to create dense clumps. Details of our simulations can be found in § 2. Our primary assumptions are that the SN ejecta can be described by a broken power law, that the maximum ejecta velocity is  $30,000 \text{ km s}^{-1}$ , that the hydrodynamics can be described by an adiabatic index  $\gamma_{ad} = 5/3$  throughout the evolution, that the wall is a constant density, and that the CSM interior to the wall is low enough density that it can be ignored.

In this manuscript, we limit our analysis of the simulation suite to hydrodynamic properties of the shock: the evolution of the forward shock front radius, evolution of shock front speeds, deceleration of the ejecta, mass of shocked material, and amount of mixing between the shocked ejecta and CSM. Details of our analysis methods can be found in § 3.1. Our main conclusions are as follows.

1. The initial ratio of the CSM density to the density of outer ejecta,  $A_0$  governs the evolution of the shock (§ 3). This is in line with Dwarkadas (2005).
2. When the reverse shock reaches ejecta of similar density to  $\rho_{wall}$  the self-similar solution applies for describing hydrodynamic properties (§ 3.4 & 3.5). This occurs later for higher- $A_0$  models.
3. We find a simple function for forward shock radius while inside the wall with parameters that depend on  $A_0$  (§ 3.2, Figures 4 & 5).
4. At late times, the shock radius evolves as a power law, so a deceleration parameter ( $m$ ) can be measured (§ 3.2, Figure 6). We find that  $m$  only indicates the CSM density profile  $s$  if  $A_0$  is very low; for higher values of  $A_0$ ,  $\eta$  and  $F_R$  change  $m$  as much as  $s$  does (Figure 7).

5. The thickness of the shocked gas grows to  $\sim 20\%$  of the forward shock radius by  $\sim 2t_{\text{imp}}$ , independent of  $A_0$ , CSM configuration, or SN type. However, at early times, it grows rapidly, which should be taken into account when estimating the volume of shocked gas (§ 3.3, Figure 8).
6. The reverse shock traverses the ejecta faster for a higher  $A_0$ , so the self-similar solution breaks down more quickly by reaching the inner ejecta for higher- $A_0$  models (Figures 3, 10, 11). Taken together with the point 2 above, the self-similar solution has a much more limited time frame of applicability in high- $A_0$  situations.
7. The deceleration of the ejecta is significantly greater from higher walls than would be calculated from the self-similar solution (§ 3.5, Figure 10). Observations of delayed-interaction SNe may indicate  $A_0 > 100$  is common.
8. The fraction of shocked ejecta within the total shocked material varies with  $A_0$  and time. Especially at early times, it cannot be assumed that the same mass of ejecta has been shocked as CSM – for high  $A_0$  it may be only 10% (§ 3.6, Figure 11).
9. The fraction of shocked CSM that has ejecta mixed into it varies with  $A_0$  and time (§ 3.7, Figure 12). Generally, at least 10% of shocked CSM is polluted by ejecta at the  $\geq 1\%$  level.
10. Applying our models to SN 2014C, under the assumption  $\eta = 4$  we find the VLBI observations agree most with a wall having  $11 \lesssim A_0 \lesssim 200$  and outer CSM of  $s = 2$  (§ 4.1).
11. We suggest that radio rise of SN 2014C is due to rapid shock acceleration after wall crossing, in

which case the wall mass is only  $M_{\text{wall}} = 0.04 - 0.31 M_{\odot}$ , much lower than derived by M17 (§ 4.2).

12. We tested the effect of the wall on late-time hydrodynamics for a few models, and find that the difference in shock radius and radius time evolution are comparable to observational error. However, the shock may be measurably wider even at late times when a wall is present (§ 4.3).

The most directly applicable observations for comparing to our results are those of very long baseline interferometry (VLBI), which unfortunately requires that the SN be very nearby. Optical line profiles have in the past been used to infer the bulk gas speed of shocked material, which can be compared to the shocked gas speeds presented here. In a sequel paper we will compute continuum radiation for this model suite, which will enable a wider array of quantitative comparisons to observation. We anticipate that the insight gained from the hydrodynamic behaviors presented here will be useful when interpreting the features of those light-curves.

#### ACKNOWLEDGEMENTS

The authors thank Paul Duffell for assistance with using RT1D and helpful discussions. The authors would like to acknowledge Raffaella Margutti, Dan Milisavljevic, Daniel Kasen, Ken Shen, Laura Chomiuk, Sumit Sabaadhicary, and Sean Couch for helpful discussions during the preparation of the manuscript, and the helpful comments of the anonymous reviewer. Simulations were run on Sparky, a workstation funded by the Department of Energy Computational Science Graduate Fellowship (CEH).

CEH acknowledges the Anishinaabek as the caretakers of the land on which she undertakes her work.

*Software:* RT1D (Duffell 2016), SciPy (Jones et al. 2001), Numpy (Oliphant 2006), Astropy (Astropy Collaboration et al. 2013), Matplotlib (Hunter 2007)

#### REFERENCES

- Anderson, G. E., Horesh, A., Mooley, K. P., Rushton, A. P., Fender, R. P., Staley, T. D., Argo, M. K., Beswick, R. J., Hancock, P. J., Pérez-Torres, M. A., Perrott, Y. C., Plotkin, R. M., Pretorius, M. L., Rumsey, C., & Titterton, D. J. 2017, MNRAS, 466, 3648
- Arcavi, I., Gal-Yam, A., Kasliwal, M. M., Quimby, R. M., Ofek, E. O., Kulkarni, S. R., Nugent, P. E., Cenko, S. B., Bloom, J. S., Sullivan, M., Howell, D. A., Poznanski, D., Filippenko, A. V., Law, N., Hook, I., Jönsson, J., Blake, S., Cooke, J., Dekany, R., Rahmer, G., Hale, D., Smith, R., Zolkower, J., Velur, V., Walters, R., Henning, J., Bui, K., McKenna, D., & Jacobsen, J. 2010, ApJ, 721, 777

- Astropy Collaboration, Robitaille, T. P., Tollerud, E. J., Greenfield, P., Droettboom, M., Bray, E., Aldcroft, T., Davis, M., Ginsburg, A., Price-Whelan, A. M., Kerzendorf, W. E., Conley, A., Crighton, N., Barbary, K., Muna, D., Ferguson, H., Grollier, F., Parikh, M. M., Nair, P. H., Unther, H. M., Deil, C., Woillez, J., Conseil, S., Kramer, R., Turner, J. E. H., Singer, L., Fox, R., Weaver, B. A., Zabalza, V., Edwards, Z. I., Azalee Bostroem, K., Burke, D. J., Casey, A. R., Crawford, S. M., Dencheva, N., Ely, J., Jenness, T., Labrie, K., Lim, P. L., Pierfederici, F., Pontzen, A., Ptak, A., Refsdal, B., Servillat, M., & Streicher, O. 2013, *A&A*, 558, A33
- Bartel, N., Bietenholz, M. F., Rupen, M. P., Beasley, A. J., Graham, D. A., Altunin, V. I., Venturi, T., Umana, G., Cannon, W. H., & Conway, J. E. 2002, *ApJ*, 581, 404
- Bietenholz, M. F., Kamble, A., Margutti, R., Milisavljevic, D., & Soderberg, A. 2018, *MNRAS*, 475, 1756
- Blandford, R. D. & Ostriker, J. P. 1978, *ApJ*, 221, L29
- Bloom, J. S., Kasen, D., Shen, K. J., Nugent, P. E., Butler, N. R., Graham, M. L., Howell, D. A., Kolb, U., Holmes, S., Haswell, C. A., Burwitz, V., Rodriguez, J., & Sullivan, M. 2012, *ApJL*, 744, L17
- Castor, J., McCray, R., & Weaver, R. 1975, *ApJL*, 200, L107
- Chevalier, R. A. 1982, *ApJ*, 258, 790
- Chevalier, R. A. & Liang, E. P. 1989, *ApJ*, 344, 332
- Chevalier, R. A. & Soker, N. 1989, *ApJ*, 341, 867
- Chomiuk, L., Soderberg, A. M., Moe, M., Chevalier, R. A., Rupen, M. P., Badenes, C., Margutti, R., Fransson, C., Fong, W.-f., & Dittmann, J. A. 2012, *ApJ*, 750, 164
- Chugai, N. N. & Chevalier, R. A. 2006, *ApJ*, 641, 1051
- Cocke, W. J., Disney, M. J., & Taylor, D. J. 1969, *Nature*, 221, 525
- Dilday, B., Howell, D. A., Cenko, S. B., Silverman, J. M., Nugent, P. E., Sullivan, M., Ben-Ami, S., Bildsten, L., Bolte, M., Endl, M., Filippenko, A. V., Gnat, O., Horesh, A., Hsiao, E., Kasliwal, M. M., Kirkman, D., Maguire, K., Marcy, G. W., Moore, K., Pan, Y., Parrent, J. T., Podsiadlowski, P., Quimby, R. M., Sternberg, A., Suzuki, N., Tytler, D. R., Xu, D., Bloom, J. S., Gal-Yam, A., Hook, I. M., Kulkarni, S. R., Law, N. M., Ofek, E. O., Polishook, D., & Poznanski, D. 2012, *Science*, 337, 942
- Dimitriadis, G., Chiotellis, A., & Vink, J. 2014, *MNRAS*, 443, 1370
- Duffell, P. C. 2016, *ApJ*, 821, 76
- Dwarkadas, V. V. 2005, *ApJ*, 630, 892
- Dwarkadas, V. V., Dewey, D., & Bauer, F. 2010, *MNRAS*, 407, 812
- Ghavamian, P., Laming, J. M., & Rakowski, C. E. 2007, *ApJL*, 654, L69
- Graham, M. L., Harris, C. E., Fox, O. D., Nugent, P. E., Kasen, D., Silverman, J. M., & Filippenko, A. V. 2017, *ApJ*, 843, 102
- Graham, M. L., Harris, C. E., Nugent, P. E., Maguire, K., Sullivan, M., Smith, M., Valenti, S., Goobar, A., Fox, O. D., Shen, K. J., Kelly, P. L., McCully, C., Brink, T. G., & Filippenko, A. V. 2019, *ApJ*, 871, 62
- Harris, C. E., Nugent, P. E., & Kasen, D. N. 2016, *ApJ*, 823, 100
- Hunter, J. D. 2007, *Computing in Science & Engineering*, 9, 90
- Jones, Eric, O. T. P. P. et al. 2001, SciPy: Open source scientific tools for Python, [Online; accessed {today}]
- Kasen, D. 2010, *ApJ*, 708, 1025
- Maoz, D., Mannucci, F., & Nelemans, G. 2014, *ARA&A*, 52, 107
- Margutti, R., Kamble, A., Milisavljevic, D., Zapartas, E., de Mink, S. E., Drout, M., Chornock, R., Risaliti, G., Zauderer, B. A., Bietenholz, M., Cantiello, M., Chakraborti, S., Chomiuk, L., Fong, W., Grefenstette, B., Guidorzi, C., Kirshner, R., Parrent, J. T., Patnaude, D., Soderberg, A. M., Gehrels, N. C., & Harrison, F. 2017, *ApJ*, 835, 140
- Milisavljevic, D., Margutti, R., Kamble, A., Patnaude, D. J., Raymond, J. C., Eldridge, J. J., Fong, W., Bietenholz, M., Challis, P., Chornock, R., Drout, M. R., Fransson, C., Fesen, R. A., Grindlay, J. E., Kirshner, R. P., Lunnan, R., Mackey, J., Miller, G. F., Parrent, J. T., Sanders, N. E., Soderberg, A. M., & Zauderer, B. A. 2015, *ApJ*, 815, 120
- Moore, K. & Bildsten, L. 2012, *ApJ*, 761, 182
- Moriya, T. J., Maeda, K., Taddia, F., Sollerman, J., Blinnikov, S. I., & Sorokina, E. I. 2013, *MNRAS*, 435, 1520
- Oliphant, T. 2006, *A guide to NumPy*
- Ramirez-Ruiz, E., García-Segura, G., Salmonson, J. D., & Pérez-Rendón, B. 2005, *ApJ*, 631, 435
- Rybicki, G. B. & Lightman, A. P. 1979, *Radiative processes in astrophysics* (Wiley-VCH)
- Silverman, J. M., Nugent, P. E., Gal-Yam, A., Sullivan, M., Howell, D. A., Filippenko, A. V., Pan, Y.-C., Cenko, S. B., & Hook, I. M. 2013, *ApJ*, 772, 125
- Smartt, S. J. 2009, *ARA&A*, 47, 63
- Staelin, D. H. & Reifstein, Edward C., I. 1968, *Science*, 162, 1481
- Tinsley, B. M. 1980, *FCPh*, 5, 287
- Tinyanont, S., Lau, R. M., Kasliwal, M. M., Maeda, K., Smith, N., Fox, O. D., Gehrz, R. D., De, K., Jencson, J., Bally, J., & Masci, F. 2019, *ApJ*, 887, 75
- Wagoner, R. V. 1977, *ApJ*, 214, L5

Weaver, R., McCray, R., Castor, J., Shapiro, P., & Moore,  
R. 1977, ApJ, 218, 377

Weiler, K. W., Panagia, N., Montes, M. J., & Sramek,  
R. A. 2002, ARA&A, 40, 387  
Wood-Vasey, W. M., Wang, L., & Aldering, G. 2004, ApJ,  
616, 339